# Platinum nanoparticles encapsulated in nitrogen-doped graphene quantum dots: Enhanced electrocatalytic reduction of oxygen by nitrogen dopants

**Limei Chen [a], Yi Peng [a], Jia-En Lu [a], Nan Wang [b], Peiguang Hu [a], Bingzhang Lu [a], Shaowei Chen [a,\*]**

[a] Department of Chemistry and Biochemistry, University of California, 1156 High Street, Santa Cruz, CA 95064, USA
[b] New Energy Research Institute, School of Environment and Energy, South China University of Technology, Guangzhou Higher Education Mega Center, Guangzhou, 510006, China

## ARTICLE INFO

## ABSTRACT

Nitrogen-doped graphene quantum dots (NGQDs) prepared by hydrothermal treatment of citric acid and urea were used as an effective support for platinum nanoparticles synthesized by carbon monoxide reduction of Pt(IV) in water. TEM measurements showed that the platinum nanoparticles were $2.03 \pm 0.43$ nm in diameter, and wrapped with one layer of NGQDs, as compared to results from AFM measurements. XPS measurements confirmed the formation of metallic platinum and the incorporation of nitrogen dopants within the graphitic molecular skeleton, and the shifts of Pt 4f binding energy suggested that charge transfer from Pt to NGQDs was facilitated by the more electronegative nitrogen dopants, as compared to platinum nanoparticle supported on undoped GQDs (Pt-GQDs). Because of this, the Pt-NGQDs nanocomposites showed markedly enhanced catalytic activity towards oxygen reduction reactions in alkaline media, as compared to Pt-GQDs, with a specific activity more than three times that of commercial Pt/C. Further comparison with NGQDs-supported gold nanoparticles showed that the platinum nanoparticles, rather than the NGQDs, played a dominant role in determining the ORR activity.

© 2017 Hydrogen Energy Publications LLC. Published by Elsevier Ltd. All rights reserved.

## Introduction

Alkaline anion-exchange membrane fuel cells have been attracting extensive attention due to high activity and durability of metal nanoparticle catalysts in alkaline media, where platinum has been recognized as the best single-metal catalyst for oxygen reduction reaction (ORR) at the cathode [1,2]. Yet a large loading of Pt is generally required due to the sluggish kinetics of ORR, which results in high costs. In order to further enhance the catalytic efficiency of Pt (and thus reduce the loading of Pt), it is generally believed that the interactions between Pt and oxygen species need to be weakened slightly, according to the so-called volcano plot

---

[3]. In other words, the binding should be strong enough to activate the dissociation of $O_2$ but not too strong to release the final products ($OH^-$) from the catalyst surface [4]. Towards this end, substantial progress has been made in the development of platinum-based ORR catalysts, and it has been found that the electronic interactions between Pt nanoparticles and the supporting substrates may be exploited as a powerful variable in the manipulation of the electronic structure of Pt and the eventual catalytic performance [5–8].

Of these, graphene derivatives have been used rather extensively due to high electrical conductivity, large surface area and good dispersion of nanoparticle catalysts [9–12]. In a series of recent studies, functional nanocomposites based on metal nanoparticles supported on graphene quantum dots (GQDs) have been prepared and the electronic interactions between GQDs and metal nanoparticles are found to modify the electronic structures of the metal nanoparticles and the eventual catalytic activity. For instance, GQDs have been prepared by acid oxidation and exfoliation of the nanometer-sized $sp^2$ domains of pitch carbon fibers, and used as substrate supports for the dispersion of platinum nanoparticles (2.5–3.5 nm in diameter) synthesized by a facile hydrothermal reduction method [6,13]. Note that the optimal size of platinum nanoparticles for ORR was predicted to be 2.3 nm, based on the calculations of oxygen binding energy for nanoparticles of varied sizes within the context of edge site concentration and coordination number [14]. Despite the larger size of the platinum nanoparticles, the resulting Pt/GQD composite exhibited much enhanced ORR activity, even compared to commercial Pt/C. This was accounted for by the GQD structural defects that induced charge transfer from Pt. Significantly, the ORR activity was found to reach a maximum when the concentration of the structural defects was about 20%. In these earlier studies, the structural defects primarily entailed oxygenated moieties in GQDs. Formation of defects may also be achieved by controlled doping with heteroatoms into the graphitic molecular skeletons. For instance, with a higher electron affinity, the incorporation of nitrogen dopants may impart a positive charge on neighboring carbon atoms [15–17], which is anticipated to further enhance charge transfer from the supported platinum nanoparticles and facilitate the control of the binding of oxygen intermediates to Pt surface, a critical process in the enhancement and optimization of the electrocatalytic activity of Pt nanoparticles for ORR [15,18].

Herein, smaller platinum nanoparticles of ca. 2 nm in diameter were prepared by CO reduction of Pt(IV) precursors in the presence of N-doped GQDs (NGQDs) that were synthesized by hydrothermal treatment of citric acid and urea. Results from TEM and AFM measurements showed that the platinum nanoparticles were capped by one single layer of NGQDs. Electrochemical studies showed that the electrocatalytic activity towards ORR was ca. 3 times higher than that of commercial Pt/C. In comparison to the Pt nanoparticles supported on undoped GQDs and gold nanoparticles supported on NGQDs, the results highlight the significance of heteroatom doping of graphene support in the manipulation of the electronic structures of nanoparticle catalysts and optimization of the ORR activity.

## Experimental section

### Chemicals

Platinum(IV) chloride ($PtCl_4$, 99%, ACROS), gold(III) chloride ($AuCl_3$, 99%, ACROS), citric acid monohydrate (99.5%, Fisher Scientific), urea (99%, Fisher Scientific), pitch carbon fibers (Fiber Glass Development Corporation), sodium carbonate ($Na_2CO_3$, $\geq$99.5%, Fisher Scientific), potassium hydroxide (KOH, Fisher Scientific), sulfuric acid ($H_2SO_4$, Fisher Scientific), nitric acid ($HNO_3$, Fisher Scientific), and Pt/C catalysts (20 wt%, Alfa Aesar) were used as received. Water was supplied by a Barnstead Nanopure water system (18.3 M $\Omega$ cm). Carbon monoxide (CO) was purchased from Airgas USA LLC. All solvents were purchased at their highest purity and used as received.

### Synthesis of NGQDs

NGQDs were prepared by adopting a procedure published previously [19,20]. In brief, 0.21 g (1 mmol) of citric acid and 0.18 g (3 mmol) of urea were dissolved in 5 mL of Nanopure water and then transferred into a 20 mL Teflon-lined autoclave. The sealed autoclave was then heated at 160 °C for 4 h. After it was cooled down to room temperature, the resulting solution was dialyzed for 3 d, affording purified NGQDs that were readily dispersible in water.

### Synthesis of (undoped) GQDs

GQDs were synthesized by exfoliation of pitch carbon fibers in concentrated acid, as described previously [21]. In brief, pitch carbon fibers (0.3 g) were added to a mixture of concentrated $HNO_3$ (20 mL) and $H_2SO_4$ (60 mL) in a round-bottom flask and sonicated for 2 h to allow for dispersion in the acids. The solution was then thermally refluxed at 100 °C for 24 h. After being cooled down to room temperature, the solution was neutralized with diluted NaOH and $Na_2CO_3$ solutions. The mixture was then purified by dialysis in Nanopure water for 3 d. The final products, GQDs, were collected by rotary evaporation, which were also highly dispersible in water.

### Synthesis of NGQDs or GQDs supported metal nanoparticles

Pt-NGQDs and Pt-GQDs nanocomposites were prepared by CO reduction of Pt(IV) precursors in the presence of NGQDs and GQDs, respectively [22,23]. In a typical experiment, 0.1 mmol of $PtCl_4$ was first dissolved in 5 mL of $H_2O$ in a 20 mL glass vial. 19.5 mg of the NGQDs prepared above was then added to the solution at a metal:carbon mass ratio of 1:1, and the mixture was bubbled with CO for 30 min under magnetic stirring. The vial was then sealed and under stirring overnight. The precipitates produced were collected by centrifugation and rinsed with water. The purified product was denoted as Pt-NGQDs. As control experiments, NGQDs-supported Au nanoparticles (Au-NGQDs) and GQDs supported Pt nanoparticles (Pt-GQDs) were prepared in the same manner. Both Pt-NGQDs and Pt-GQDs were readily dispersible in the mixture of ethanol and water (10:1 v/v) showing a red purple color, but not in pure

water, whereas Au-NGQDs could only be suspended in the ethanol/water mixture, as shown in Fig. S1.

### Structural characterizations

TEM studies were carried out with a JEOL JEM-2010 TEM microscope operated at 200 kV. X-ray photoelectron spectra (XPS) were recorded with a PHI 5400 XPS instrument equipped with an Al K$_\alpha$ source operated at 350 W and at $10^{-9}$ Torr. Dynamic light scattering (DLS) measurements were carried out with a Wyatt Protein Solution Dynapro Temperature Controlled Microsampler. Raman spectra were recorded on a LabRAM HR Evolution with a 514.5 nm laser. AFM measurements were carried out under ambient conditions with a Molecular Imaging PicoLE SPM instrument. FTIR spectra were obtained with a Perkin-Elmer FTIR spectrometer (Spectrum One, spectral resolution 4 cm$^{-1}$), where the samples were prepared by casting the sample solutions onto a ZnS disk. UV–vis absorption spectra were collected with a PerkinElmer Lambda 35 UV–vis spectrometer.

### Electrochemistry

Electrochemical studies were carried out in a standard three-electrode cell connected to a CHI-710 electrochemical workstation, with a Pt foil counter electrode and a reversible hydrogen electrode (RHE) reference electrode at room temperature (21 °C). The working electrode was a rotating ring-disk electrode (RRDE, with a glassy carbon disk and a gold ring, Pine Instrument). In a typical measurement, a calculated amount of the nanocomposites prepared above (at *ca.* 1 mg of metal content), 3.4 mg of Vulcan XC72 carbon powders, and 10 μL of a Nafion solution were ultrasonically mixed in 1 mL of an ethanol/water mixture. Then 10 μL of this solution was dropcast onto the glassy-carbon disk (5.61 mm in diameter) with a 10 μL autopipette. As soon as the electrode was dried, a dilute Nafion solution (0.1 wt%, 3 μL) was added onto it, and the electrode was immersed into electrolyte solutions for voltammetric measurements. The metal loading on the electrode was estimated to be 10 μg in all samples.

## Results and discussion

### Structural characterization

Fig. 1 shows the representative TEM images of (A, B) Pt-NGQDs and (C, D) Pt-GQDs nanocomposites. It can be seen that in both samples, the platinum nanoparticles are dispersed rather homogeneously without significant agglomeration. For Pt-NGQDs, the majority of the Pt nanoparticles are in the range of 1.0–3.0 nm with an average of 2.03 ± 0.43 nm in diameter, as manifested in the core size histogram in the inset to panel (A). Furthermore, from high-resolution TEM image in panel (B), lattice fringes can be identified with a spacing of 0.199 nm, which is consistent with the (200) crystalline planes of *fcc* Pt (PDF 04-0802). Similar characteristics can be seen with the Pt-GQDs counterparts, as depicted in panels (C) and (D), where the majority of the nanoparticles are within the range of 1.2–3.7 nm, with an average diameter of 2.29 ± 0.50 nm. It

should be mentioned that the sizes of these Pt nanoparticles are close to the optimal core size (2.3 nm) of Pt nanoparticles predicted by theoretical calculations [14] but somewhat smaller than those of Pt-GQDs nanocomposites (ca. 3 nm in dia.) prepared previously by hydrothermal reduction of Pt(II) [6,24], and commercial Pt/C (3.30 ± 0.42 nm) [25]. As for the Au-NGQDs nanocomposites (Fig. S2), the gold nanoparticles were markedly larger in a broad range of 20–70 nm, with an average diameter of 38.85 ± 10.72 nm, and displayed well-defined lattice fringes with an interplanar spacing of 0.235 nm that is consistent with the Au(111) planes (PDF 04-0784).

Due to the low crystallinity and electron-density of NGQDs and GQDs, it was difficult to resolve the graphene derivatives in TEM measurements. Yet, the formation of a composite structure was confirmed in AFM and DLS measurements. From the AFM topographs in Fig. 2(A$_1$) and (B$_1$), one can see good dispersion of both samples, consistent with results from TEM measurements (Fig. 1), and line scans in panels (A$_2$) and (B$_2$) showed no obvious difference of the thickness of the two composites, mostly between 3 and 4 nm. Statistical analysis based on more than 100 nanoparticles showed the average thickness was 3.81 ± 1.43 nm for Pt-NGQDs and 3.84 ± 1.18 nm for Pt-GQDs, as depicted in panels (A$_3$) and (B$_3$), respectively. Since the metal core diameters were 2.03 ± 0.43 nm for Pt-NGQDs and 2.29 ± 0.50 nm for Pt-GQDs (Fig. 1), this suggests that in the composites, the Pt nanoparticles were stabilized with a capping layer of ca. 0.9 nm and 0.8 nm, respectively, very close to the average thickness of NGQDs (0.97 ± 0.51 nm) [19] and GQDs (0.99 ± 0.34 nm) (Fig. S3). It is likely that such a capping layer of NGQDs or GQDs rendered the corresponding nanocomposites readily dispersible in the mixture of water and ethanol (Fig. S1). Consistent results were obtained in DLS measurements, where the average hydrodynamic radii of Pt-NGQDs and Pt-GQDs were estimated to be 20.3 and 12.0 nm, respectively, markedly higher than those of NGQDs (1.68 nm) and GQDs (5.24 nm).

The optical properties of the nanocomposites were then examined by UV–vis measurements. From Fig. 3, it can be seen that in comparison with the largely featureless profile of GQDs, an absorption band emerged at 335 nm with the NGQDs sample, which can be assigned to the n → π* transition of conjugated C−N/C=N moieties [19]. This peak can also be observed with the Pt-NGQDs sample, but the intensity was markedly reduced, likely due to the preferential deposition of Pt nanoparticles onto the defect sites (i.e., oxygenated and nitrogen dopant moieties) [6]. Additionally, a broad absorption band can be seen at ca. 530 nm for both Pt-NGQDs and Pt-GQDs composites, which might be ascribed to residual CO species adsorbed on the platinum particle surface [26], consistent with results from FTIR measurements (Fig. S4). For the Au-NGQDs sample, a strong absorption peak was observed at 550 nm (Fig. S5), most probably a combined contribution from the surface plasmon resonance of the gold nanoparticles and adsorbed CO species [27].

The chemical composition and valence states of Pt-NGQDs and Pt-GQDs nanocomposites were further examined by XPS measurements. Fig. 4(A) depicts the survey spectra of Pt-GQDs and Pt-NGQDs, where three main peaks can be identified at around 75, 285 and 532 eV, corresponding to the Pt 4f, C 1s and O 1s electrons, respectively, for both Pt-GQDs and Pt-NGQDs,
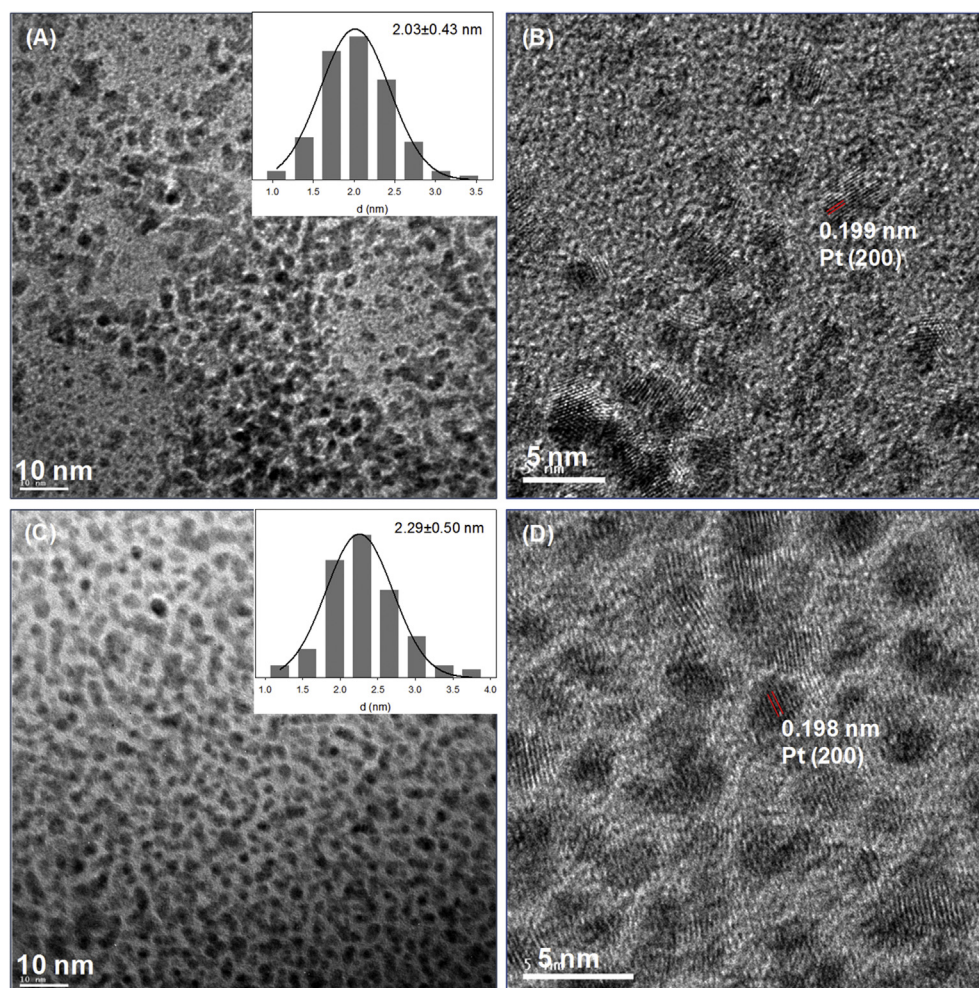
Fig. 1 — Representative TEM images of (A, B) Pt-NGQDs and (C, D) Pt-GQDs. The insets to panels (A) and (C) are the corresponding core size histograms.

while an additional peak can be seen at around 400 eV for Pt-NGQDs that is ascribed to the N 1s electrons (the two peaks within the range of 100–150 eV are ascribed to the Si 2p and Si 2s electrons from the silicon wafer substrate). The high-resolution scans of the C 1s electrons are depicted in Fig. 4(B) and (E) for Pt-GQDs and Pt-NGQDs, respectively. It can be seen from Fig. 4(B) that the C 1s spectrum of Pt-GQDs can be deconvoluted into three peaks at 284.0 eV, 284.8 eV, and 287.2 eV, which may be assigned to $sp^2$ hybridized carbon (C=C), $sp^3$ hybridized C (C—C) and oxidized carbon (C=O), respectively, indicating that GQDs were indeed decorated with oxygenated moieties, as observed previously [20,28,29]. These three carbon species can also be identified with Pt-NGQDs in panel (E), but at slightly higher binding energies of 284.3 eV, 285.1 eV, and 287.6 eV [20,28,29], likely due to electron withdrawing from the more electronegative nitrogen dopants [16]. In fact, from the N 1s spectrum of Pt-NGQDs (panel D), three major components can be identified by deconvolution at ca. 398.1 eV, 399.6 eV and 401.0 eV, which can be assigned to the pyridinic, pyrrolic, and graphitic N, respectively [19,30]. This suggests that nitrogen was indeed doped into the graphitic matrix. The Pt 4f spectrum was depicted in panel (C), where the binding energies of Pt 4f electrons can be found at 71.5 and

74.8 eV for the Pt-GQDs composite, consistent with those of metallic platinum [24,31]. In contrast, the Pt 4f binding energies were somewhat higher at 71.8 and 75.1 eV for Pt-NGQDs (panel F), suggesting increasing charge transfer from Pt to the supporting NGQDs. Note that in computational studies based on DFT calculations, the carbon atoms adjacent to nitrogen dopants have been found to possess a positive charge density, due to the strong electronic affinity of the nitrogen dopant [32,33]. Since these structural defects are the preferential anchoring sites for platinum nanoparticle deposition [6], the resulting intimate interactions most likely facilitated electron transfer from the Pt nanoparticles, leading to an increase of the Pt binding energy. In fact, this is consistent with results from FTIR measurements (Fig. S4), where the vibrational energy of residual CO was higher with Pt-NGQDs than with Pt-GQDs, because a decreased Pt electron density in the former diminished back-donation of the metal d electrons to the CO $\pi^*$ orbital, leading to an enhanced bonding order of CO.

In addition, based on the integrated peak areas, the total concentration of N dopants was calculated to be 12.1 at.% in Pt-NGQDs, of which 20.9% was pyridinic N, 46.8% was pyrrolic N and 32.3% was graphitic N. That is, p-type doping (pyridinic and pyrrolic N) accounts for the majority of the N dopants
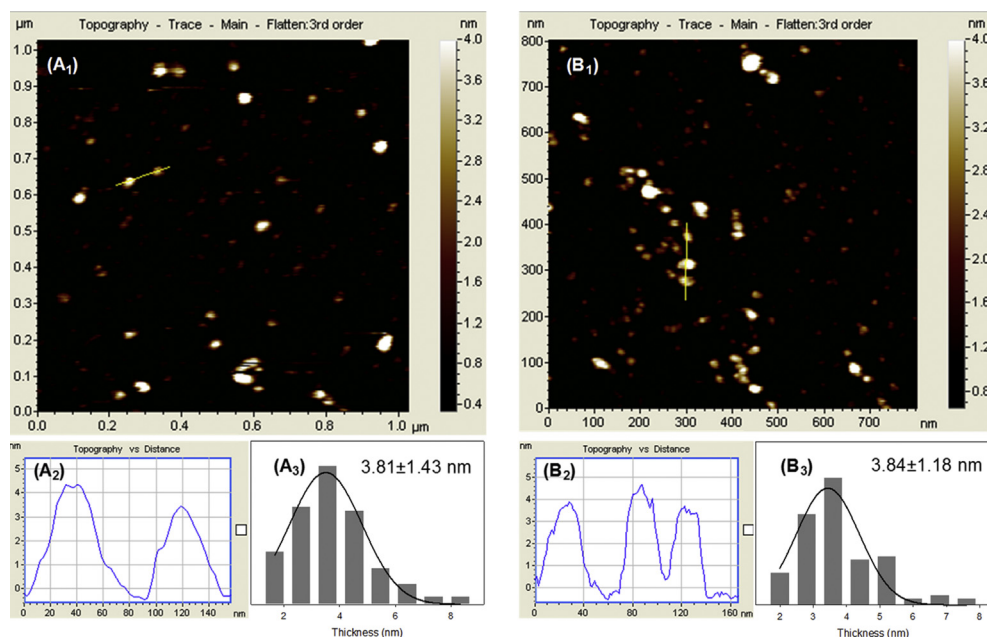
**Fig. 2 −** Representative AFM topographs of (A₁) Pt-NGQDs and (B₁) Pt-GQDs. Panels (A₂) and (B₂) depict the height profiles along the lines in (A₁) and (A₂), respectively. The corresponding thickness distributions are shown in panels (A₃) and (B₃).

[34−37]. Consistent results were obtained with Au-NGQDs (Fig. S6). The mass loading of Pt in Pt-NGQDs and Pt-GQDs was found to be very close at 61.0 wt% and 62.3 wt%, respectively, whereas the gold content was somewhat lower at 16.6 wt% in Au-NGQDs. Furthermore, of all carbons, $sp^2$ carbons accounted for 56.3% in Pt-NGQDs, and 50.9% for Pt-GQDs, indicating that the graphene supports were actually rather defective. This is in good agreement with results from Raman measurements, where both Pt-NGQDs and Pt-GQDs exhibited well-defined D and G bands (Fig. S7), characteristic of graphene derivatives. Yet, the vibrational energies are somewhat different, at 1380 and 1588 $cm^{-1}$ for Pt-GQDs and 1381 and 1608 $cm^{-1}$ for Pt-NGQDs, where the blue shift (ca. 20 $cm^{-1}$) of

the G band energy in the latter as compared to the former is consistent with nitrogen doping that modified the electronic structure of the graphitic skeletons [38−40]. In addition, the ratio of the integrated areas of the D and G-bands was estimated to be 0.90 and 1.66 for Pt-NGQDs and Pt-GQDs, respectively, signifying that NGQDs were less defective than GQDs, in good agreement with results from XPS measurements.

*Electrochemical study*

The electrocatalytic activity of the Pt-NGQDs, Pt-GQDs and Au-NGQDs nanocomposites towards ORR were then examined and compared, with Pt/C as the benchmark materials. Fig. 5 shows the steady-state cyclic voltammograms of a glassy carbon electrode modified with a certain amount of the series of catalysts in a nitrogen-saturated 0.1 M KOH solution. All samples exhibited the typical voltammograms of platinum. From the figure, one can see that a pair of broad voltammetric peaks appeared within the potential range of +0.6 to +1.0 V. These are due to OH adsorption on Pt in the anodic scan forming $PtO_x$ and oxide reduction in the return sweep. For Pt-NGQDs, the peak potential for $PtO_x$ formation was ca. +0.84 V, which was more positive than that for Pt-GQDs (+0.82 V) and Pt/C (+0.83 V). A similar variation can be seen in the peak potential for oxide reduction in the anodic scan. This suggests that the oxygen affinity decreased in the order of Pt-GQDs ≥ Pt/C > Pt-NGQDs, a feature that would have significant implication in their ORR performance (*vide infra*). In addition, two more pairs of voltammetric peaks appeared between +0.15 and +0.50 V, due to hydrogen adsorption/desorption on the platinum surface, and based on the integrated areas, the effective electrochemical surface area (ECSA) of the nanoparticle catalysts was estimated to be 15.7 $m^2/g_{Pt}$ for Pt/C, 12.7 $m^2/g_{Pt}$ for Pt-GQDs and 15.2 $m^2/g_{Pt}$ for Pt-NGQDs.
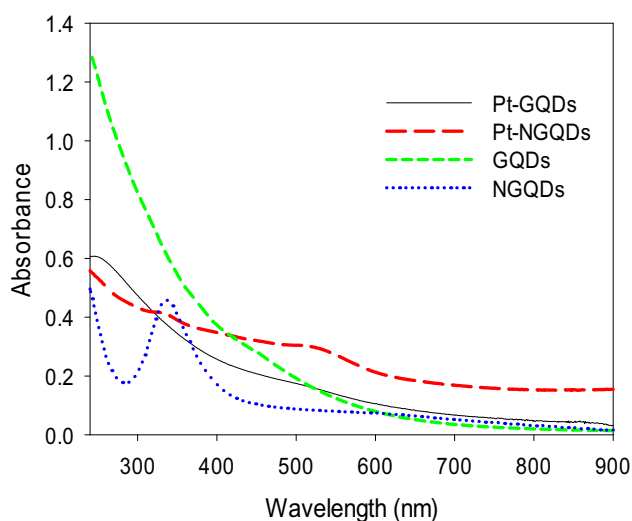


**Fig. 3 −** UV−vis absorption spectra of Pt-NGQDs and Pt-GQDs in water:ethanol (10:1 v:v), and NGQDs and GQDs in water.
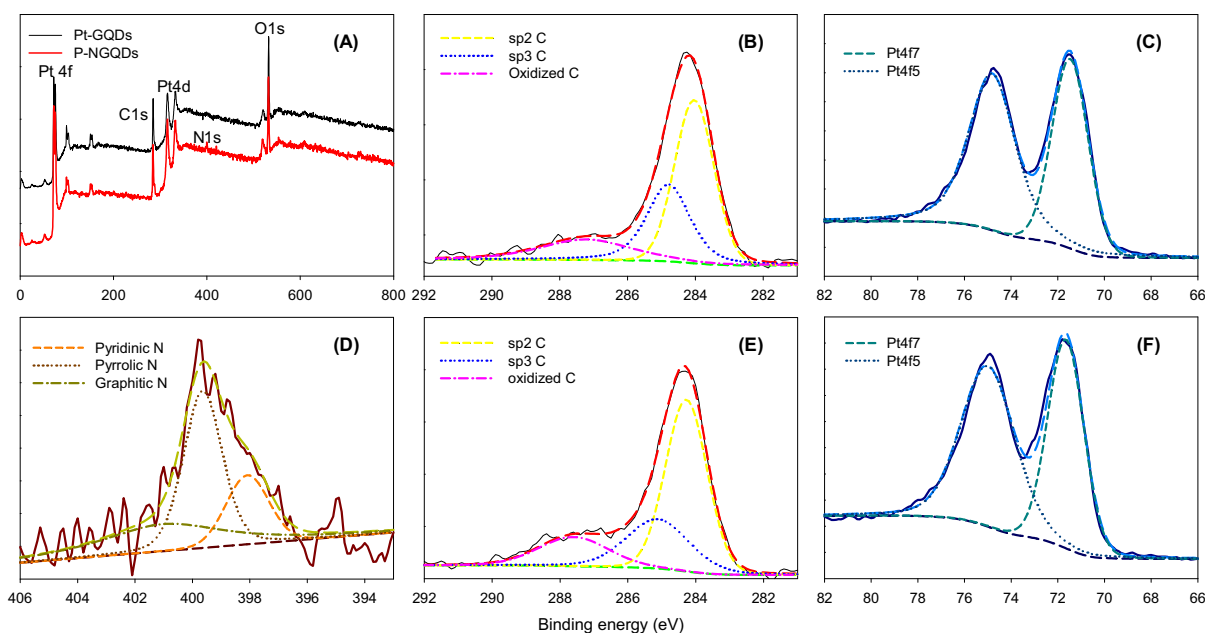
Fig. 4 − (A) XPS survey spectra of Pt-GQDs (black curve) and Pt-NGQDs (red curve), and the corresponding high-resolution scans of (B) C 1s and (C) Pt 4f electrons of Pt-GQDs, and (D) N 1s, (E) C 1s and (F) Pt 4f electrons of Pt-NGQDs. solid curves are experimental data and dotted/dashed curves are deconvolution fits. (For interpretation of the references to colour in this figure legend, the reader is referred to the web version of this article.)

The electrocatalytic activity in oxygen reduction was then examined by rotating (ring) disk voltammetric measurements with the KOH solution saturated with oxygen. Fig. 6(A) depicts the representative RDE voltammograms of the glassy carbon disk electrode modified with commercial Pt/C, Pt-GQDs, Pt-NGQDs or Au-NGQDs composites at the rotation rate of 1600 rpm within the potential range of +0.4−1.1 V (vs. RHE). It can be seen that when the potential was swept negatively, nonzero currents started to emerge at all samples, suggesting apparent electrocatalytic activity towards ORR. Yet the half-wave potentials are markedly different, at ca. +0.84 V for Pt/C, +0.85 V for Pt-GQDs, +0.90 V
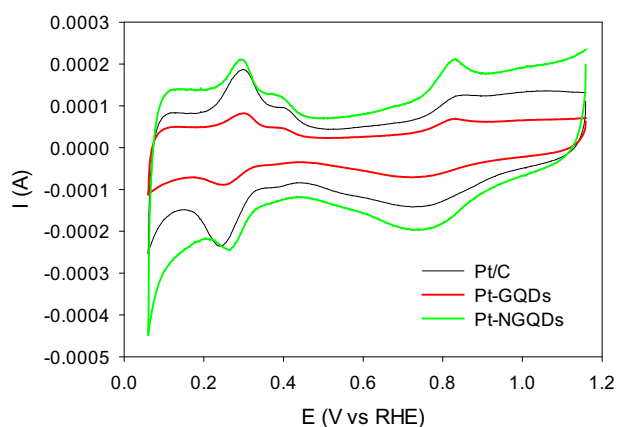
for Pt-NGQDs, and +0.74 V for Au-NGQDs; furthermore, the limiting currents also varied substantially, at 1.24 mA, 0.75 mA, 1.38 mA, and 0.84 mA, respectively. A similar behavior can be observed with the kinetic current densities (specific activity), which were quantitatively estimated by normalizing the kinetic currents obtained from the y-axis intercepts of the linear regressions of the Koutecky-Levich plots (Fig. S8) to the corresponding ECSA. From the Tafel plot in Fig. 6(B), one can see that at all samples the specific activity increased with increasingly negative potential. Apparently, the specific activity of Pt-NGQDs is significantly higher than those of the other samples within the entire potential range (+0.7 to +1.0 V). For instance, at +0.90 V, the specific activity was estimated to be 1.03 A/m$^2$ for Pt/C, 1.03 A/m$^2$ for Pt-GQDs, 4.22 A/m$^2$ for Pt-NGQDs, and undetectable for Au-NGQDs. That is, the specific activity of Pt-NGQDs was 4.1 times higher than that of Pt/C. A consistent variation can be observed at +0.85 and +0.95 V, as depicted in panel (C). In terms of mass activity, both Pt-NGQDs and Pt-GQDs were also markedly better than commercial Pt/C, with Pt-NGQDs remaining the best among the series (Fig. S9). Nevertheless, the Tafel slopes were found to be almost invariant at 116 mV/dec for Pt/C, 106 mV/dec for Pt-GQDs, 131 mV/dec for Pt-NGQDs, and 126 mV/dec for Au-NGQDs, indicating that the first electron transfer to oxygen was likely the rate determining for all composite catalysts [11,24].

Moreover, by setting the ring potential at +1.5 V, the ring currents were collected (Fig. S8) to quantitatively estimate the amounts of peroxide intermediates produced. This is manifested in the number of electron transfer (n) during oxygen reduction, $n = \frac{4 I_{disk}}{I_{disk} + I_{ring}/N}$, where $I_{disk}$ and $I_{ring}$ are the voltammetric currents at the disk and ring electrode, respectively, and N is the collection efficiency (40%) [11]. As depicted in



Fig. 5 − Cyclic voltammograms of an RRDE electrode modified with Pt/C, Pt-GQDs and Pt-NGQDs in a nitrogen-saturated 0.1 M KOH solution. Potential scan rate 20 mV/s. Pt loadings were 10.0 μg (Pt/C), 12.4 μg (Pt-GQDs) and 12.2 μg (Pt-NGQDs).
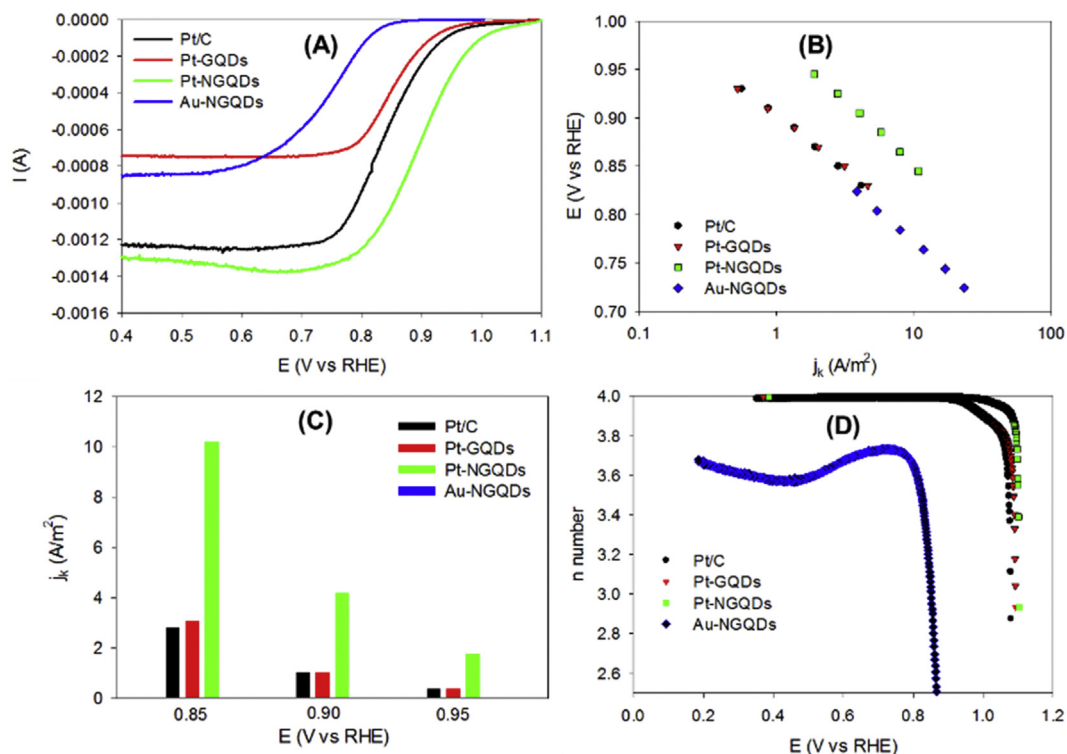
Fig. 6 — (A) RDE voltammograms of the Pt/C, Pt-GQDs, Pt-NGQDs and Au-NGQDs nanocomposites in oxygen-saturated 0.1 M KOH at the electrode rotation rate of 1600 rpm. (B) Tafel plots of the nanocomposites. (C) Comparison of the specific activities (kinetic current densities) at +0.85, +0.90 and +0.95 V (vs RHE) among the catalysts. (D) Variation of the number of electron transfer (n) with electrode potentials.

Fig. 6(D), Pt-NGQDs, Pt-GQDs, and Pt/C all exhibited n ≈ 4 at potentials below +0.9 V, indicating complete reduction of $O_2$ to $OH^-$, whereas the n values were somewhat lower at 3.6 to 3.8 for Au-NGQDs.

Taken together, these results indicate that the Pt-NGQDs composite stood out as the best ORR catalyst among the series, and the performance was actually highly comparable to, or even better than, leading results reported in recent literature with relevant catalyst systems based on platinum nanoparticles supported on graphene derivatives and commercial Pt/C (Table S1), within the context of onset potential, specific activity, and mass activity. In addition, one may notice that Pt-NGQDs performed much better than Pt-GQDs, suggesting that nitrogen doping might be exploited as additional structural defects in the manipulation of Pt electron density and hence the interactions with oxygen species [41], consistent with results from XPS (Fig. 4) and FTIR (Fig. S4) measurements. Furthermore, the fact that the ORR activity of Pt-NGQDs was markedly better than that of Au-NGQDs indicates that Pt nanoparticles, rather than the N-doped GQDs, played a dominant role in determining the electrocatalytic performance. This has also been observed previously with Pd nanoparticles supported on nitrogen-doped GQDs [11]. Note that such a remarkable performance was achieved with the size of the platinum nanoparticles close to the optimal value predicted by theoretical calculations [14], where the reduced size might facilitate metal-support interfacial interactions [42,43].

## Conclusions

In this study, nanocomposites based on platinum nanoparticles (2.03 ± 0.43 nm in diameter) supported on NGQDs were successfully prepared by carbon monoxide reduction of $PtCl_4$ in the presence of NGQDs. The resulting Pt-NGQD nanocomposites exhibited markedly enhanced electrocatalytic activity in oxygen reduction as compared to the undoped counterparts (Pt-GQDs), gold nanoparticle-NGQDs nanocomposites, as well as commercial Pt/C. Significantly, whereas oxygen was found to undergo four electron reduction to $OH^-$ at all Pt-based catalysts, the Pt-NGQDs composites exhibited a most positive half-wave potential at +0.90 V, and a specific activity that was more than 4 times that of Pt/C. This remarkable performance was accounted for by charge transfer from Pt to the positively charged carbon atoms in NGQDs that was facilitated by the more electronegative nitrogen dopants, which led to a decrease of the binding energy of oxygen species to Pt surface. The results further highlights the significance of interfacial electron transfer in the manipulation and optimization of nanoparticle catalytic activity towards ORR [8].

## Acknowledgements

## Appendix A. Supplementary data

Supplementary data related to this article can be found at https://doi.org/10.1016/j.ijhydene.2017.10.078.

REFERENCES

[1] Matsumoto K, Fujigaya T, Yanagi H, Nakashima N. Very high performance alkali anion-exchange membrane fuel cells. Adv Funct Mater 2011;21:1089–94.

[2] Park JS, Park SH, Yim SD, Yoon YG, Lee WY, Kim CS. Performance of solid alkaline fuel cells employing anion-exchange membranes. J Power Sources 2008;178:620–6.

[3] Stephens IEL, Bondarenko AS, Gronbjerg U, Rossmeisl J, Chorkendorff I. Understanding the electrocatalysis of oxygen reduction on platinum and its alloys. Energy Environ Sci 2012;5:6744–62.

[4] Greeley J, Stephens IEL, Bondarenko AS, Johansson TP, Hansen HA, Jaramillo TF, et al. Alloys of platinum and early transition metals as oxygen reduction electrocatalysts. Nat Chem 2009;1:552–6.

[5] Wang CM, Ma L, Liao LW, Bai S, Long R, Zuo M, et al. A unique platinum-graphene hybrid structure for high activity and durability in oxygen reduction reaction. Sci Rep 2013;3:2580.

[6] Song Y, Chen SW. Graphene quantum-dot-supported platinum nanoparticles: defect-mediated electrocatalytic activity in oxygen reduction. ACS Appl Mater Interfaces 2014;6:14050–60.

[7] Lim DH, Wilcox J. Mechanisms of the oxygen reduction reaction on defective graphene-supported Pt nanoparticles from first-principles. J Phys Chem C 2012;116:3653–60.

[8] Peng Y, Lu BZ, Wang N, Li LG, Chen SW. Impacts of interfacial charge transfer on nanoparticle electrocatalytic activity towards oxygen reduction. Phys Chem Chem Phys 2017;19:9336–48.

[9] Fei H, Dong J, Arellano-Jimenez MJ, Ye G, Dong Kim N, Samuel EL, et al. Atomic cobalt on nitrogen-doped graphene for hydrogen generation. Nat Commun 2015;6:8668.

[10] Jhong HM, Tornow CE, Smid B, Gewirth AA, Lyth SM, Kenis PJ. A nitrogen-doped carbon catalyst for electrochemical CO$_2$ conversion to CO with high selectivity and current density. ChemSusChem 2017;10:1094–9.

[11] Deming CP, Mercado R, Lu JE, Gadiraju V, Khan M, Chen SW. Oxygen electroreduction catalyzed by palladium nanoparticles supported on nitrogen-doped graphene quantum dots: impacts of nitrogen dopants. ACS Sustain Chem Eng 2016;4:6580–9.

[12] Hu PG, Liu K, Deming CP, Chen SW. Multifunctional graphene-based nanostructures for efficient electrocatalytic reduction of oxygen. J Chem Technol Biotechnol 2015;90:2132–51.

[13] Gan ZX, Xiong SJ, Wu XL, Xu T, Zhu XB, Gan X, et al. Mechanism of photoluminescence from chemically derived graphene oxide: role of chemical reduction. Adv Opt Mater 2013;1:926–32.

[14] Shao MH, Peles A, Shoemaker K. Electrocatalysis on platinum nanoparticles: particle size effect on oxygen reduction reaction activity. Nano Lett 2011;11:3714–9.

[15] Li MT, Zhang LP, Xu Q, Niu JB, Xia ZH. N-doped graphene as catalysts for oxygen reduction and oxygen evolution reactions: theoretical considerations. J Catal 2014;314:66–72.

[16] Zhang JT, Dai LM. Heteroatom-doped graphitic carbon catalysts for efficient electrocatalysis of oxygen reduction reaction. ACS Catal 2015;5:7244–53.

[17] Jukk K, Kongi N, Rauwel P, Matisen L, Tammeveski K. Platinum nanoparticles supported on nitrogen-doped graphene nanosheets as electrocatalysts for oxygen reduction reaction. Electrocatalysis 2016;7:428–40.

[18] Fan MM, Zhu CL, Yang JZ, Sun DP. Facile self-assembly N-doped graphene quantum dots/graphene for oxygen reduction reaction. Electrochim Acta 2016;216:102–9.

[19] Chen LM, Hu PG, Deming CP, Wang N, Lu JE, Chen SW. Intervalence charge transfer of ruthenium-nitrogen moieties embedded within nitrogen-doped graphene quantum dots. J Phys Chem C 2016;120:13303–9.

[20] Qu D, Zheng M, Zhang LG, Zhao HF, Xie ZG, Jing XB, et al. Formation mechanism and optimization of highly luminescent N-doped graphene quantum dots. Sci Rep 2014;4:5294.

[21] Deming CP, Mercado R, Gadiraju V, Sweeney SW, Khan M, Chen SW. Graphene quantum dots-supported palladium nanoparticles for efficient electrocatalytic reduction of oxygen in alkaline media. ACS Sustain Chem Eng 2015;3:3315–23.

[22] Hu PG, Chen LM, Deming CP, Bonny LW, Lee HW, Chen SW. Identification of the formation of metal-vinylidene interfacial bonds of alkyne-capped platinum nanoparticles by isotopic labeling. Chem Commun 2016;52:11631–3.

[23] Surendran G, Apostolescu G, Tokumoto M, Prouzet E, Ramos L, Beaunier P, et al. From self-assembly of platinum nanoparticles to nanostructured materials. Small 2005;1:964–7.

[24] He GQ, Song Y, Liu K, Walter A, Chen S, Chen SW. Oxygen reduction catalyzed by platinum nanoparticles supported on graphene quantum dots. ACS Catal 2013;3:831–8.

[25] Zhou ZY, Kang XW, Song Y, Chen SW. Ligand-mediated electrocatalytic activity of Pt nanoparticles for oxygen reduction reactions. J Phys Chem C 2012;116:10592–8.

[26] Rabilloud F, Harb M, Ndome H, Archirel P. UV-visible absorption spectra of small platinum carbonyl complexes and particles: a density functional theory study. J Phys Chem A 2010;114:6451–62.

[27] Creighton JA, Eadon DG. Ultraviolet visible absorption-spectra of the colloidal metallic elements. J Chem Society Faraday Trans 1991;87:3881–91.

[28] Liu F, Jang MH, Ha HD, Kim JH, Cho YH, Seo TS. Facile synthetic method for pristine graphene quantum dots and graphene oxide quantum dots: origin of blue and green luminescence. Adv Mater 2013;25:3657–62.

[29] Luk CM, Chen BL, Teng KS, Tang LB, Lau SP. Optically and electrically tunable graphene quantum dot-polyaniline composite films. J Mater Chem C 2014;2:4526–32.

[30] Liu YH, Wang RT, Lang JW, Yan XB. Insight into the formation mechanism of graphene quantum dots and the size effect on their electrochemical behaviors. Phys Chem Chem Phys 2015;17:14028–35.

[31] Dablemont C, Lang P, Mangeney C, Piquemal JY, Petkov V, Herbst F, et al. FTIR and XPS study of Pt nanoparticle functionalization and interaction with alumina. Langmuir 2008;24:5832–41.

[32] Gong KP, Du F, Xia ZH, Durstock M, Dai LM. Nitrogen-doped carbon nanotube arrays with high electrocatalytic activity for oxygen reduction. Science 2009;323:760—4.

[33] Saidi WA. Oxygen reduction electrocatalysis using N-doped graphene quantum-dots. J Phys Chem Lett 2013;4:4160—5.

[34] Schiros T, Nordlund D, Palova L, Prezzi D, Zhao LY, Kim KS, et al. Connecting dopant bond type with electronic structure in N-doped graphene. Nano Lett 2012;12:4025—31.

[35] Fujimoto Y, Saito S. Formation, stabilities, and electronic properties of nitrogen defects in graphene. Phys Rev B 2011;84.

[36] Hou ZF, Wang XL, Ikeda T, Terakura K, Oshima M, Kakimoto M. Electronic structure of N-doped graphene with native point defects. Phys Rev B 2013;87.

[37] Kim HS, Kim HS, Kim SS, Kim YH. Atomistic mechanisms of codoping-induced p- to n-type conversion in nitrogen-doped graphene. Nanoscale 2014;6:14911—8.

[38] Mandal TK, Hou Y, Gao ZY, Ning HR, Yang WS, Gao MY. Graphene oxide-based sensor for ultrasensitive visual detection of fluoride. Adv Sci 2016;3, 1600217.

[39] Lv R, Li Q, Botello-Mendez AR, Hayashi T, Wang B, Berkdemir A, et al. Nitrogen-doped graphene: beyond single substitution and enhanced molecular sensing. Sci Rep 2012;2:586.

[40] Panchokarla LS, Subrahmanyam KS, Saha SK, Govindaraj A, Krishnamurthy HR, Waghmare UV, et al. Synthesis, structure, and properties of boron- and nitrogen-doped graphene. Adv Mater 2009;21:4726—30.

[41] Stamenkovic VR, Mun BS, Arenz M, Mayrhofer KJ, Lucas CA, Wang G, et al. Trends in electrocatalysis on extended and nanoscale Pt-bimetallic alloy surfaces. Nat Mater 2007;6:241—7.

[42] Ma JW, Habrioux A, Luo Y, Ramos-Sanchez G, Calvillo L, Granozzi G, et al. Electronic interaction between platinum nanoparticles and nitrogen-doped reduced graphene oxide: effect on the oxygen reduction reaction. J Mater Chem A 2015;3:11891—904.

[43] Su FB, Tian ZQ, Poh CK, Wang Z, Lim SH, Liu ZL, et al. Pt nanoparticles supported on nitrogen-doped porous carbon nanospheres as an electrocatalyst for fuel cells. Chem Mater 2010;22:832—9.